# Stability Analysis and Key Parameters Design for Grid-Connected Current-Source Inverter With Capacitor-Voltage Feedback Active Damping

Yiwen Geng, Xuanfeng Song, Xu Zhang, Ke Yang, and Haiwei Liu

***Abstract*—In a three-phase grid-connected current-source inverter system with the capacitor-voltage feedback (CVF)-based active damping method, a high-pass filter is usually employed in the CVF loop to mitigate its impact on system dynamics. Meanwhile, the inherent delays in a digital control system brought by pulsewidth modulation (PWM) and the digital control will make stability analysis and parameters design of the control system more complicated. In this article, the impacts of the high-pass filter and the inherent delays are considered for stability analysis and parameters design. The impacts of the cutoff frequency of the high-pass filter and the CVF damping coefficient on the system stability are analyzed in the discrete domain, and an optimal CVF damping coefficient is obtained. Moreover, a key parameters design method for the control system is proposed. The method simplifies the procedure of key parameters designing, which can mitigate the resonance of the system caused by the CL filter effectively with better dynamics and steady state performance. Finally, simulation and experimental results are provided to verify the effectiveness of the proposed method in this article.**

***Index Terms*—Active damping, CL resonance, capacitor-voltage feedback (CVF), current-source inverter, parameters design, stability analysis.**

## I. Introduction

CURRENT-SOURCE inverters (CSIs) can be widely found in many applications such as renewable power generation [1], [2], motor drive systems [3], [4], and active power filters [5]. Compared with voltage-source inverters (VSIs), CSIs have several advantages such as boost capacity, reliable short-circuit protection capacity, and direct-current control capacity.

Fig. 1 shows the typical topology of a three-phase CSI in grid-connected system. The inverter is intended to provide pure sinusoidal grid-connected current with low total harmonic distortion. A common practice to reduce the switching harmonics caused by pulsewidth modulation (PWM) is to insert a *CL* filter between the terminal of the inverter and the common ac bus. The presence of the *CL* filter brings the risk of harmonic resonance and may destabilize the system. The methods of suppressing the harmonic resonance can be categorized as the passive damping approach and the active damping approach. The passive damping approach utilizes a damping resistor in series or shunt with the filter capacitor or inductor. Though they are robust, the passive damping methods sometimes introduce unacceptable power loss, particularly in high-power applications. The active damping approach, on the other hand, involves only change in the control loops and does not bring additional power loss. Several different damping methods have been proposed to damp the resonance actively in recent years. In [6], the input filter resonance of current-source rectifier is actively mitigated by feedforward control signal compensation using the *LC* filter model. The control signal shaping method with different compensations is proposed in [7]–[9], requiring minimum design effort by being simply embedded into the existing control loop. However, the damping methods mentioned above are sensitive to resonant frequency variations. In practical grid-connected CSI systems, the *CL* resonant frequency will vary in a wide range due to the existence of grid impedance. Hence, the virtual impedance method [10]–[13] is suitable for such a CSI system for it is immune to resonant frequency variations. In recent years, the inductor-current feedback (ICF)-based active damping method and the capacitor-voltage feedback (CVF)-based active damping method have been proposed. In [14], the transfer functions of the *CL* filter-based grid-connected CSI system with ICF control and CVF control were studied separately. The study indicated that only the proportional CVF control and the derivative ICF control can damp the resonance. Compared to proportional CVF control, the derivative element of derivative ICF control is hardly achieved physically since it is a lead element. Moreover, a

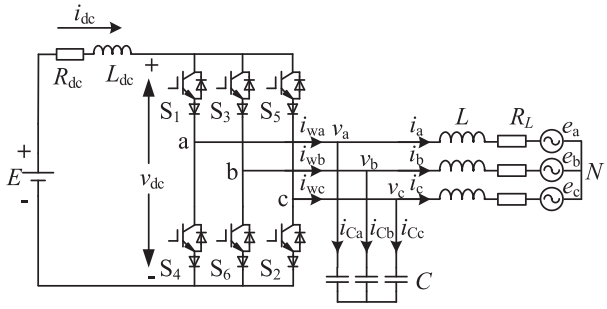


Fig. 1. Topology of a three-phase grid-connected CSI.

Manuscript received March 7, 2020; revised August 17, 2020; accepted October 28, 2020. Date of publication November 6, 2020; date of current version February 5, 2021. Recommended for publication by Associate Editor B.G. Fernandes. *(Corresponding author: Xuanfeng Song.)*

The authors are with the School of Electrical and Power Engineering, China University of Mining and Technology, Xuzhou 221116, China (e-mail: 13913475362@139.com; songfeng_ok@163.com; 18361232578@163.com; 13056203255@163.com; 15062116124@163.com).

Color versions of one or more of the figures in this article are available online at https://ieeexplore.ieee.org.

Digital Object Identifier 10.1109/TPEL.2020.3036187

low-pass filter is normally required in the feedback loop in practical applications [14], which makes the control system more complicated. Therefore, the active damping method based on proportional CVF control is adopted in this article.

The impacts of the inherent delays brought by PWM and digital control, and the high-pass filter utilized in the CVF loop should be focused when carrying out stability analysis and parameters design for a CSI system. The work in [15] demonstrated that the delay cannot be ignored for analyzing the harmonic resonance between the converter and its output filter. The work in [16] shows that digital control and PWM contribute to one sampling period delay and half a sampling period delay separately, and create an overall 1.5 sampling period delay, which will have an impact on the active damping method. In [17], the impact of the inherent delays on the stability of an off-grid VSI system were analyzed in detail. The result shows that if the resonant frequency of the filter $f_r$ and the sampling frequency $f_s$ satisfy $f_r > f_s/3$, the inherent delays can mitigate the resonance caused by the filter without active damping methods. Otherwise, an active damping method must be employed to stabilize the system. The work in [18] shows that CSI and VSI are dual in topology, which demonstrates that the conclusions in [17] are also suitable for the analysis of a grid-connected CSI system. In addition, a high-pass filter is usually required in the CVF loop to eliminate the fundamental component of the feedback signal. Otherwise, the amplitude of the feedback signal will be excessive and affect the system dynamics [19]. The work in [20] has considered the impact of the high-pass filter when analyzing system stability and designing control parameters for a CSI system, but ignored the impact of inherent delays. The work in [21] and [22] has considered the impact of control delays but ignored the impact of the high-pass filter. However, the work above has not considered the relationship between damping coefficient, controller, and system stability when designing system parameters with the consideration of high-pass filter and inherent delay.

Motivated by the aforementioned limitation, this article presents a detailed model of a grid-connected CSI system with the proportional CVF-based active damping method based on PR control in the discrete domain. The impacts of the high-pass filter utilized in the feedback loop and the 1.5 sampling period delay brought by PWM and digital control on the system stability are investigated. Based on the analysis, the effective region of the CVF coefficient is obtained when the closed-loop system is stable. Furthermore, a key parameter design method is proposed to design the key parameters of the control system, involving the CVF damping coefficient, the proportional gain and the resonant gain of the PR controller. The proposed method simplifies the designing procedure of the key parameters of the control system with excellent system dynamics and effective resonance mitigation. Finally, simulation and experimental results are presented to show the effectiveness of the proposed method in this article.

## II. Mathematical Model of Three-Phase Grid-Connected CSI

Fig. 1 shows the typical topology of a three-phase grid-connected CSI system, which consists of a constant dc-link power source, a dc-side filter inductor $L_{dc}$ with its parasitic resistance $R_{dc}$, a three-phase full-bridge CSI, and a *CL* filter. It is noted that a CSI requires a forward series diode on each IGBT to obtain reverse voltage withstand capability. In Fig. 1, $C$, $L$, and $R_L$ are the filter capacitor, the filter inductor, and the parasitic resistance of the filter inductor, respectively. $i_{dc}$ is the dc-side current and $E_{dc}$ is the dc-link voltage. $i_{wk}$, $i_k$, and $i_{Ck}$ ($k = a, b, c$) are the inverter-side current, grid-side current, and the capacitor current, respectively. $v_k$ and $e_k$ ($k = a, b, c$) are the capacitor voltage and the grid-side voltage, respectively. Since the parasitic resistance of the filter inductor in the *CL* filter will provide some damping in the system, the parasitic resistance is neglected to concern the worst condition of the system [18].

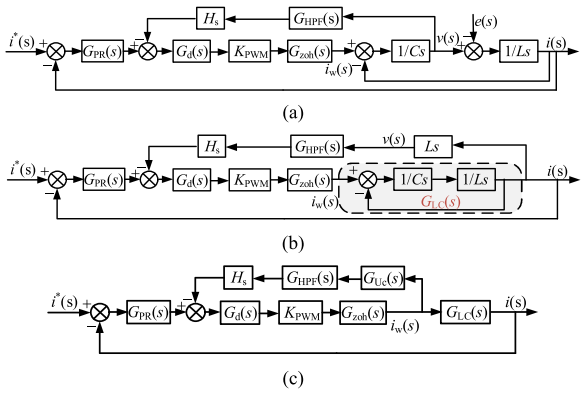


Fig. 2. $s$-domain model of a CSI system with proportional CVF-based active damping method in the stationary $\alpha\beta$-system. (a) Original $s$-domain model. (b) Process of simplification. (c) Simplified $s$-domain model.

Fig. 2(a) shows the original $s$-domain model of a grid-connected CSI system with a proportional CVF-based active damping method in the stationary $\alpha\beta$-system, where $H_s$ is the proportional CVF damping coefficient. $K_{PWM}$ is the PWM gain of the inverter. $G_d(s)$ presents the digital control delay caused by sampling and computing [15]. $G_{zoh}(s)$ is the transfer function of the zero-order hold (ZOH), which is an inherent property of the PWM modulator [17]. $G_d(s)$ and $G_{zoh}(s)$ can be given in $s$-domain by

$$\begin{cases} G_d(s) = e^{-sT_s} \\ G_{zoh}(s) = \frac{1-e^{-sT_s}}{T_s s} \end{cases} \tag{1}$$

where $T_s$ is the sampling period.

$G_{HPF}(s)$ is the high-pass filter in the CVF control loop, which is used to mitigate its impact on the system dynamics. the $s$-domain transfer function of it can be given by

$$G_{HPF}(s) = \frac{s}{s+\omega_c} \tag{2}$$

where $\omega_c$ is the cutoff angular frequency of the high-pass filter, and its corresponding cutoff frequency $f_c$ can be expressed as $\omega_c = 2\pi f_c$.

The control structure shown in Fig. 2(a) can be simplified into Fig. 2(b) and (c). $G_{LC}$ $(s)$ is the transfer function from the inverter-side current $i_w(s)$ to the grid-connected current $i(s)$, which can be expressed as

$$G_{LC}(s) = \frac{i\,(s)}{i_w\,(s)} = \frac{\omega_r^2}{s^2+\omega_r^2}. \tag{3}$$

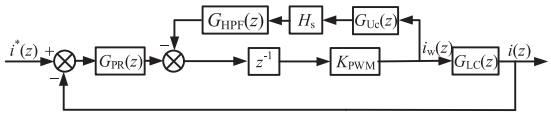


Fig. 3. $z$-domain model of a grid-connected CSI system with proportional CVF-based active damping method.

$G_{\mathrm{Uc}}(s)$ is the transfer function from the inverter current $i_{\mathrm{w}}(s)$ to the capacitor-voltage $v(s)$, which can be expressed as

$$G_{Uc}(s) = \frac{v(s)}{i_{\mathrm{w}}(s)} = \frac{1}{sC} \cdot \frac{s^2}{s^2 + \omega_{\mathrm{r}}^2}. \tag{4}$$

In (3) and (4), $\omega_{\mathrm{r}}$ is the resonant angular frequency of the *CL* filter, which can be expressed as

$$\omega_{\mathrm{r}} = \frac{1}{\sqrt{CL}} = 2\pi f_{\mathrm{r}} \tag{5}$$

where $f_{\mathrm{r}}$ is the resonant frequency of the *CL* filter.

A proportional and resonant (PR) controller is employed to track the sinusoidal current reference in the stationary $\alpha\beta$-system. The $s$-domain transfer function of the PR controller can be expressed as

$$G_{\mathrm{PR}}(s) = k_{\mathrm{p}} + k_{\mathrm{r}} \frac{\omega_{\mathrm{b}} s}{s^2 + 2\omega_{\mathrm{b}} s + \omega_0^2} \tag{6}$$

where $k_{\mathrm{p}}$ is the proportional gain, $k_{\mathrm{r}}$ is the resonance gain, $\omega_0$ is the fundamental angular frequency of the grid, and $\omega_{\mathrm{b}}$ is the bandwidth of the PR controller.

The control structure diagram shown in Fig. 2 consists of an inner damping loop and an outer current control loop. The inner damping loop is used to mitigate the resonance caused by the *CL* filter, including the cutoff frequency of the high-pass filter and proportional CVF damping coefficient. The outer current control loop is used to track the grid-connected current reference, including the proportional gain and the resonance gain of the PR controller. It is difficult to analyze the stability and design the parameters of the CSI control system due to the coupling between the inner damping loop and the outer current loop. Moreover, the inherent delays in the CSI control system caused by digital control and PWM introduce a nonlinear term $e^{-sT_s}$ according to (1), which makes the analysis and the parameters designing of the system complicated in the $s$-domain. Hence, the structure shown in Fig. 2 is studied in the $z$-domain. In Section III, the impact of the cutoff frequency of the high-pass filter and the proportional CVF damping coefficient on the system stability is analyzed in the $z$-domain. The method of the key parameter design is given in Section IV. The transfer function of the grid-connected CSI system in the $z$-domain is given in the following.

Fig. 3 shows the model of grid-connected CSI system with proportional CVF-based active damping method in the $z$-domain, where $G_{\mathrm{LC}}(z)$ and $G_{\mathrm{Uc}}(z)$ are the discrete versions of $G_{\mathrm{LC}}(s)$ and $G_{\mathrm{Uc}}(s)$ derived with the ZOH transformation

$$\begin{aligned} G_{\mathrm{LC}}(z) &= Z[G_{\mathrm{h}}(s) \cdot G_{\mathrm{LC}}(s)] \\ &= [1 - \cos(\omega_{\mathrm{r}} T_{\mathrm{s}})] \cdot \frac{z+1}{z^2 - 2z\cos(\omega_{\mathrm{r}} T_{\mathrm{s}}) + 1} \end{aligned} \tag{7}$$

$$\begin{aligned} G_{\mathrm{Uc}}(z) &= Z[G_{\mathrm{h}}(s) \cdot G_{\mathrm{Uc}}(s)] \\ &= \frac{\sin(\omega_{\mathrm{r}} T_{\mathrm{s}})}{\omega_{\mathrm{r}} C} \cdot \frac{z-1}{z^2 - 2z\cos(\omega_{\mathrm{r}} T_{\mathrm{s}}) + 1}. \end{aligned} \tag{8}$$

$G_{\mathrm{HPF}}(z)$ are the discrete versions of $G_{\mathrm{HPF}}(s)$ derived with the ZOH transformation

$$G_{\mathrm{HPF}}(z) = \frac{z-1}{z - e^{-\omega_{\mathrm{c}} T_{\mathrm{s}}}} \tag{9}$$

$G_{\mathrm{PR}}(z)$ is the discrete version of $G_{\mathrm{PR}}(s)$ by applying the prewrapped bilinear (Tustin) transformation for (5), and is obtained as

$$\begin{aligned} G_{\mathrm{PR}}(z) = k_{\mathrm{p}} &+ \frac{k_{\mathrm{r}} \omega_{\mathrm{b}} \sin(\omega_0 T_{\mathrm{s}})}{2} \\ &\cdot \frac{(z^2 - 1)}{\omega_0[z^2 + 2\cos(\omega_0 T_{\mathrm{s}})z + 1] + \omega_{\mathrm{b}} \sin(\omega_0 T_{\mathrm{s}})(z^2 - 1)}. \end{aligned} \tag{10}$$

Accordingly, the open-loop transfer function of the control system in the $z$-domain can be defined as

$$\begin{aligned} T_{\mathrm{o}}(z) &= G_{\mathrm{PR}}(z) \\ &\cdot \frac{[1 - \cos(\omega_{\mathrm{r}} T_{\mathrm{s}})](z - e^{-\omega_{\mathrm{c}} T_s})(z+1)}{z(z - e^{-\omega_{\mathrm{c}} T_s})[z^2 - 2\cos(\omega_{\mathrm{r}} T_{\mathrm{s}})z + 1] + \frac{H_{\mathrm{s}} \sin(\omega_{\mathrm{r}} T_{\mathrm{s}})}{\omega_{\mathrm{r}} C}(z-1)^2}. \end{aligned} \tag{11}$$

## III. Stability Analysis of Three-Phase Grid-Connected CSI

### A. Regions of Active Damping

In this section, the impact of the *CL* resonant frequency on the system stability is analyzed considering that the CVF-based active damping method is not employed, by setting $H_{\mathrm{s}}$ to zero. Generally, the resonance gain of the quasi-PR controller $k_{\mathrm{r}}$ can be neglected if the *CL* resonant frequency is far larger than the resonant frequency of the quasi-PR controller [23]. In such a case, $G_{\mathrm{PR}}(z)$ can be expressed as $G_{\mathrm{PR}}(z) \approx k_{\mathrm{p}}$. Therefore, the expressions of the open-loop transfer function and its phase without active damping can be expressed as

$$T_{\mathrm{so}}(z) \approx \frac{k_p K_{\mathrm{PWM}}(z+1)[1 - \cos(\omega_{\mathrm{r}} T_{\mathrm{s}})]}{z[z^2 - 2\cos(\omega_{\mathrm{r}} T_{\mathrm{s}})z + 1]} \tag{12}$$

$$\angle T_{\mathrm{so}}(z = e^{\mathrm{j}\omega T_s}) = \begin{cases} -\frac{3}{2} T_{\mathrm{s}} \omega = -3\pi T_{\mathrm{s}} f & (f < f_{\mathrm{r}}) \\ -\frac{3}{2} T_{\mathrm{s}} \omega - \pi = -3\pi T_{\mathrm{s}} f - \pi & (f > f_{\mathrm{r}}). \end{cases} \tag{13}$$

As it can be seen, there is a phase jump of $-180°$ and a resonance peak in the magnitude of $T_{\mathrm{so}}(z)$ at the resonance frequency $f_{\mathrm{r}}$. According to (13), when $f_{\mathrm{r}} < f_{\mathrm{s}}/3$, the phase angle of $T_{\mathrm{so}}(z)$ crosses $-180°$ at $f_{\mathrm{r}}$; when $f_{\mathrm{r}} > f_{\mathrm{s}}/3$, the phase angle of $T_{\mathrm{so}}(z)$ crosses $-180°$ at $f_{\mathrm{s}}/3$. Hence, in the case that $f_{\mathrm{r}} > f_{\mathrm{s}}/3$, the phase of $T_{\mathrm{so}}$(z) pass through $-180°$ before $f_{\mathrm{r}}$, and it is possible to select a gain $k_{\mathrm{p}}$ so that the magnitude of $T_{\mathrm{so}}(z)$ at the crossing frequency $f_{\mathrm{s}}/3$ is below unit. In other words, the Nyquist plot of $T_{\mathrm{so}}(z)$ can avoid encircling the critical point $(-1, j0)$ by choosing a small $k_{\mathrm{p}}$ to make the system stable. However, when $f_{\mathrm{r}} < f_{\mathrm{s}}/3$, the phase jump will make the phase of $T_{\mathrm{so}}(z)$ pass through $-180$ at $f_{\mathrm{r}}$ and lead the Nyquist plot of $T_{\mathrm{so}}(z)$ to cross

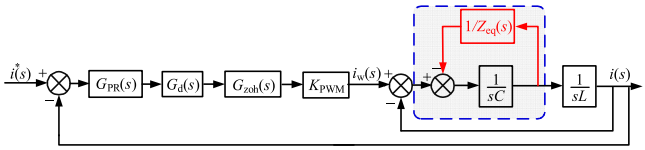


Fig. 4. Equivalent block diagram of the grid-connected CSI system with proportional CVF-based active damping.

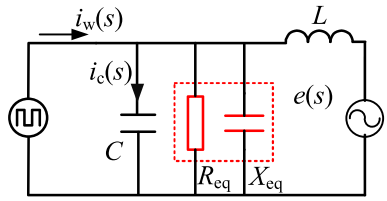


Fig. 5. Equivalent circuit model of active damping.

the negative real axis and encircle the critical point $(-1, j0)$, even with a very small $k_p$, since the magnitude of the peak will always be higher than unit. In such a case, an active damping method must be employed to ensure the system stability. In order to better mitigate the harmonic resonance, the resonant frequency $f_r$ is usually designed less than half of the switching frequency $f_{sw}$, which can be expressed as $f_r < f_{sw}/2$. In this article, the asymmetrical regular sampling mode is adopted. In such a case, the sampling frequency $f_s$ is twice the switching frequency $f_{sw}$, and the resonant frequency $f_r$ satisfies $f_r < f_s/4$. Consequently, the active damping method is necessary to employed in order to ensure the stability of the system.

### B. Physical Significance of CVF-Based Active Damping

According to the analysis above, it is necessary to utilize the active damping method to ensure the stability of the system when $f_r < f_s/4$. In this article, the proportional CVF-based active damping method is adopted.

To make a clearer explanation on the physical essence of the proportional CVF-based active damping method, the circuit model will be studied in the $s$-domain. The control structure diagram shown in Fig. 2(b) can be modified to the equivalent control structure diagram shown in Fig. 4.

As can be seen from Fig. 4, the proportional CVF-based active damping is equivalent to inserting a virtual impedance $1/Z_{eq}(s)$ in parallel with the ac-side filter capacitor. The transfer function of the virtual impedance can be obtained as

$$\frac{1}{Z_{eq}(s)} = H_s G_{HPF}(s) G_d(s) G_{zoh}(s) \approx H_s \frac{s}{s+\omega_c} e^{-1.5sT_s}. \tag{14}$$

To investigate the impact of $1/Z_{eq}(s)$ on the system stability, it can be expressed in the complex form

$$Z_{eq} = R_{eq} // jX_{eq} \tag{15}$$

$$\begin{cases} R_{eq}(\omega) = \frac{\omega^2+\omega_c^2}{H_s \omega g_R(\omega)} \\ X_{eq}(\omega) = \frac{\omega^2+\omega_c^2}{H_s \omega g_X(\omega)} \end{cases} \tag{16}$$

$$\begin{cases} g_R(\omega) = \sqrt{\omega^2+\omega_c^2}\cos(1.5\omega T_s - \theta) \\ g_X(\omega) = \sqrt{\omega^2+\omega_c^2}\sin(1.5\omega T_s - \theta) \\ \theta = \arccos \frac{\omega}{\sqrt{\omega^2+\omega_c^2}}. \end{cases} \tag{17}$$

It can be observed from (15)–(17) that the proportional CVF-based active damping loop is equivalent to inserting an equivalent resistor $R_{eq}$ and an equivalent reactance $X_{eq}$ in parallel with the filter capacitor, as shown in Fig. 5. $R_H$ is given by $R_H = 1/R_{eq}$ and $X_H$ is given by $X_H = 1/X_{eq}$. In the CSI system employing the proportional CVF-based active damping method,

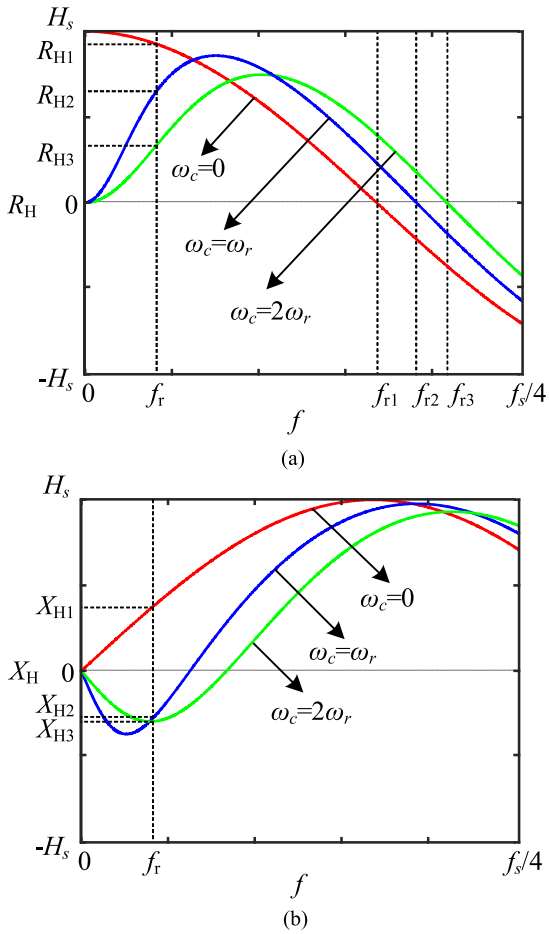


Fig. 6. Impact of the cutoff frequency of the high-pass filter on the frequency characteristic of $R_{eq}$ and $X_{eq}$. (a) Frequency characteristic of $R_{eq}$. (b) Frequency characteristic of $X_{eq}$.

the higher values of $R_H$ exhibit better damping [20]. Fig. 6 shows the impact of the cutoff frequency of the high-pass filter on the frequency characteristic of $R_H$ and $X_H$. In Fig. 6, $f_{r1}$, $f_{r2}$, and $f_{r3}$ are the values of frequency at $R_H = 0$ when $\omega_c$ is equal to zero, $\omega_r$ and $2\omega_r$, respectively. $R_{H1}$, $R_{H2}$, and $R_{H3}$ are the values of $R_H$ at $f_r$ when $\omega_c$ is equal to zero, $\omega_r$ and $2\omega_r$, respectively. $X_{H1}$, $X_{H2}$, and $X_{H3}$ are the values of $X_H$ at $f_r$ when $\omega_c$ is equal to zero, $\omega_r$ and $2\omega_r$, respectively. As can be seen from Fig. 6, with the increasing of the cutoff frequency of the high-pass filter, the region of $R_H > 0$ become bigger, i.e., the region of resonance damping become larger, meaning that the system is more robust. $X_H$ is negative at $f_r$ when employing the CVF-based active damping method, meaning that $X_{eq}$ appears to capacitive, so the actual resonant peak will be shifted to the

left side of the original resonance frequency. To expand the region of resonance damping, increasing the cutoff frequency of the high-pass filter $\omega_c$ is reasonable in theory. However, the value of $R_H$ decreases with the increasing of $\omega_c$, exhibit worse damping performance. Besides, the high-pass filter in this article is utilized to eliminate the fundamental frequency component of the capacitance voltage and make the resonant frequency component of the capacitance voltage pass as far as possible. Hence, $\omega_c$ is usually given by $\omega_r < \omega_c < 2\omega_r$. To ensure the performance of active damping, $\omega_c = \omega_r$ is adopted in this article. According to Fig. 6(a), the damping performance can become better by increasing the value of $H_s$ in theory. However, when $H_s$ is too large, the rectifier system may become unstable [21]. Hence, it is necessary to make the stability analysis of the control system considering the impact of the high-pass filter and design an optimal value of $H_s$ to ensure better robustness.

### C. Stability Analysis of Grid-Connected CSI System With CVF-Based Active Damping Method

Due to the inherent delays in the digital control system, the system becomes nonlinear, which makes it difficult to analyze the system stability in the *s*-domain. Hence, the stability analysis of the control system is studied in the *z*-domain in this article. The root locus diagram is utilized to illustrate that the stability of the open-loop system is a necessary and sufficient condition for the stability of the closed-loop system. Hence, the stability of the open-loop system is analyzed first. Equation (11) is the open-loop transfer function of the grid-connected CSI system with a proportional CVF-based active damping method in the *z*–domain. To simplify the representation, the following expressions are obtained:

$$\begin{cases} a = \cos(\omega_r T_s) \\ \beta = e^{-\omega_c T_s} \\ b = H_s \sin(\omega_r T_s)/(\omega_r C) \end{cases} \tag{18}$$

where $b$ can be regarded as the damping coefficient.

The denominator factorization of $T_o(z)$ given by (11) can be expressed as

$$\text{den}(z) = z(z-\beta)(z^2 - 2az + 1) + b(z-1)^2. \tag{19}$$

To study the stability of open-loop system, setting $z = (1 + w)/(1 - w)$ in (19) yields

$$\text{den}(w) = a_0 w^4 + a_1 w^3 + a_2 w^2 + a_3 w^1 + a_4 \tag{20}$$

where

$$\begin{cases} a_0 = 2\left[(1+a)(1+\beta) + 2b\right] \\ a_1 = 4(1 + a - 2b) \\ a_2 = 4(1 - a\beta + b) \\ a_3 = 4(1 - a) \\ a_4 = 2(1-a)(1-\beta). \end{cases} \tag{21}$$

Table I shows the Routh table for the open-loop system, where $b_1 = (a_1 a_2 - a_0 a_3)/a_1$ and $c_1 = (b_1 a_3 - a_1 a_4)/b_1$. From (18), $0 < a < 1$ and $0 < \beta < 1$ can be obtained. Hence, $a_4 > 0$ is obtained. To ensure the stability of the system, $a_0$, $a_1$, $b_1$, and $c_1$ are all required to be positive. Setting $a_0 > 0$ and $a_1 > 0$ yields

$$-\frac{(1+a)(1+\beta)}{2} < b < \frac{1+a}{2}. \tag{22}$$

To study the symbol of $c_1$, substituting $b_1 = (a_1 a_2 - a_0 a_3)/a_1$ into $b_1 a_3 - a_1 a_4 > 0$ yields

$$(a_1 a_2 - a_0 a_3) - \frac{{a_1}^2 a_4}{a_3} > 0. \tag{23}$$

For the last term in (23) satisfies ${a_1}^2 a_4/a_3 > 0$, $a_1 a_2 - a_0 a_3 > 0$ can be derived, i.e., $b_1 > 0$. Combining $b_1 > 0$ with (23), $c_1 > 0$ can be derived. Hence, $b_1 > 0$ and $c_1 > 0$ can be derived at the same time from (23). Substituting (21)–(23) yields

$$\begin{cases} 0 < b < \frac{2a-\beta}{2-\beta} (2a > \beta) \\ \frac{2a-\beta}{2-\beta} < b < 0 (2a < \beta). \end{cases} \tag{24}$$

TABLE I
ROUTH TABLE FOR OPEN-LOOP SYSTEM

| | | | |
|---|---|---|---|
| $w_4$ | $a_0$ | $a_2$ | $a_4$ |
| $w_3$ | $a_1$ | $a_3$ | 0 |
| $w_2$ | $b_1$ | $a_4$ | |
| $w_1$ | $c_1$ | 0 | |
| $w_0$ | $a_4$ | | |

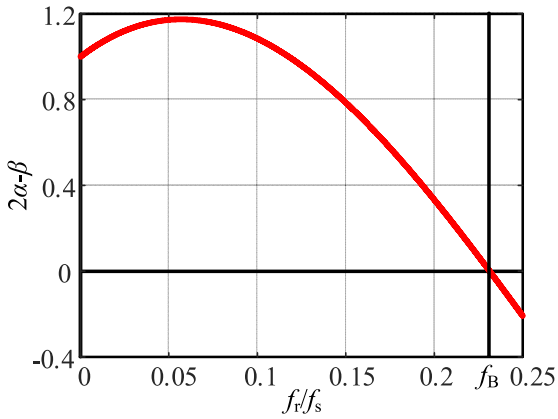


Fig. 7. Values of $2a-\beta$ at different $f_r$.

Fig. 7 shows the values of $2a-\beta$ at different resonance frequencies $f_r$. It can be observed in Fig. 7 that $2a > \beta$ can be derived when $f_r < f_B$. In this case, the stability condition of the open-loop system can be expressed as $0 < b < (2a - \beta)/(2 - \beta)$. When $f_B < f_r < f_s/4$, the resonance mitigation can be achieved by reducing the cutoff frequency of the high-pass filter based on $(2a - \beta)/(2 - \beta) < b < 0$. The stability analysis and key parameters design of the closed-loop system in the following are studied in the case that $f_r < f_B$ only for the analysis and design in the case that $f_B < f_r < f_s/4$ is similar.

In summary, when $f_r < f_B$, (24) is the necessary and sufficient condition for the stability of the open-loop system. In addition, (24) shows that the value of $(2a - \beta)/(2 - \beta)$ decreases with the increasing of $\beta$, and (18) shows that the value of $\beta$ decreases with the increasing of $\omega_c$, which means that the stability boundary of the open-loop system with a high-pass filter ($\omega_c = \omega_r$) are larger

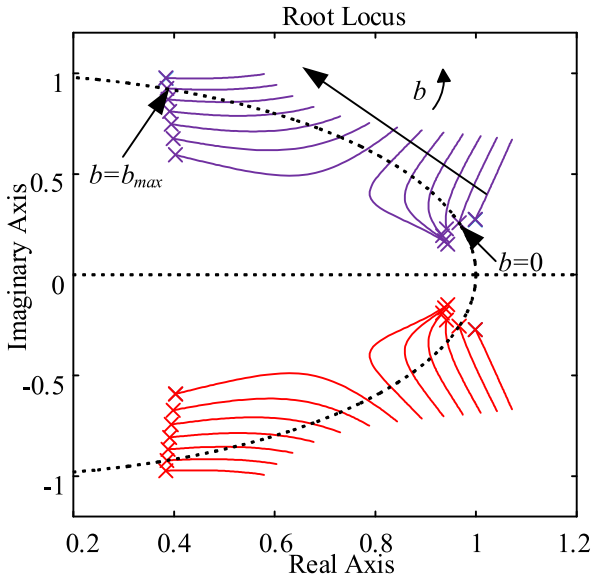


Fig. 8. Root locus diagram of the closed-loop system with $b$ varying at $f_{\mathrm{r}} = 410.9$ Hz.

than that without a high-pass filter ($\omega_{\mathrm{c}} = 0$). Hence, it is another benefit of utilizing a high-pass filter.

Then, the root locus diagram is used to illustrate that the stability of the closed-loop system is equivalent to the stability of the open-loop system. The open-loop transfer function can be simplified as

$$T_{\mathrm{o}}(z) \approx \frac{k_p(1-a)(z-\beta)(z+1)}{z(z-\beta)(z^2-2az+1)+b(z-1)^2}. \tag{25}$$

Fig. 8 depicts the root locus diagram of the closed-loop system with $f_{\mathrm{r}} = 410.9$ Hz, i.e., $C = 50\ \mu$F and $L = 3$ mH, where $b_{\max}$ is equal to $(2a-\beta)/(2-\beta)$. It can be observed in Fig. 8 that when $0 < b < b_{\max}$, the closed-loop poles can be located in the unit circle by tuning the proportional gain $k_{\mathrm{p}}$ of the PR controller to ensure the system stability. Hence, when the damping coefficient $b$ of the system dissatisfies $0 < b < b_{\max}$, there is no intersection point between the root locus and the unit circle, which means that the system cannot be stabilized by changing the value of $k_{\mathrm{p}}$. In other words, the close-loop system can be stabilized only in the case that the open-loop system is stable, i.e., the stability of the open-loop system is the necessary and sufficient condition for the stability of the closed-loop system.

In summary, the closed-loop system can be stabilized by adjusting $k_{\mathrm{p}}$ of the PR controller only in the case that the open-loop system is stable, i.e., $0 < b < (2a-\beta)/(2-\beta)$.

## IV. Key Parameters Design of Grid-Connected CSI System

The key parameters of the grid-connected CSI system with a proportional CVF-based active damping method mainly consist of the proportional CVF coefficient $H_{\mathrm{s}}$, the proportional gain $k_{\mathrm{p}}$ and the resonance gain $k_{\mathrm{r}}$ of the PR controller. In this section, the key parameters design method of the system is explained.

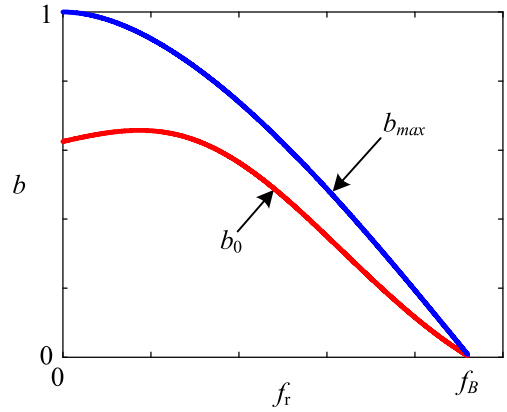


Fig. 9. Curves of $b_0$ and $b_{\max}$ with resonant frequencies varying.

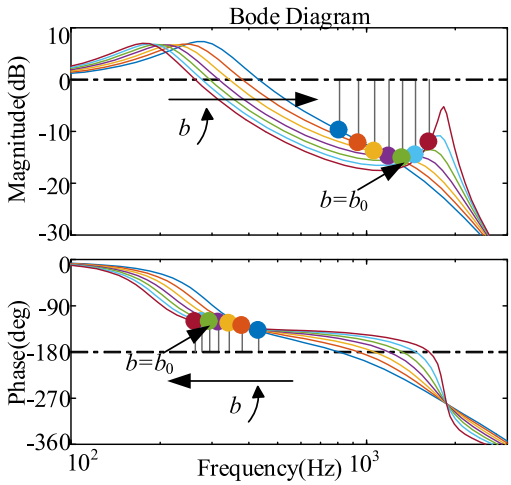


Fig. 10. Bode diagram of $T_{\mathrm{oz}}(z)$ with $b$ varying at $k_{\mathrm{p}} = 1$.

When $f_{\mathrm{r}} < f_{\mathrm{B}}$ and $0 < b < (2a-\beta)/(2-\beta)$, the closed-loop system can be stabilized by adjusting the proportional gain $k_{\mathrm{p}}$ of the PR controller (see Section II). According to the Nyquist stability criterion, the amplitude of $T_{\mathrm{o}}(z)$ should be less than 1 at $f_{\mathrm{R}}$ to ensure the system stability in the case that the phase of $T_{\mathrm{o}}(z)$ is –180° at $f_{\mathrm{R}}$. The amplitude of $T_{\mathrm{o}}(z)$ at frequency $f_{\mathrm{R}}$ can be expressed as

$$\begin{aligned} T_{\mathrm{o}}(e^{j\omega_R T_s}) &\approx \frac{k_p(1-a)(\mathrm{C}+j\mathrm{D})}{\mathrm{A}+j\mathrm{B}} \\ &= \frac{k_p(1-a)[(\mathrm{AC}+\mathrm{BD})+j(\mathrm{AD}-\mathrm{BC})]}{\mathrm{A}^2+\mathrm{B}^2} \end{aligned} \tag{26}$$

where

$$\begin{cases} \mathrm{A} = 2(x-a)(2x^2-1) + \frac{2b(x-1)(1-\beta x)}{1+\beta^2-2\beta x} \\ \mathrm{B} = 4xy(x-a) - \frac{2b(x-1)\beta y}{1+\beta^2-2\beta x} \\ \mathrm{C} = x+1 \\ \mathrm{D} = y \end{cases} \tag{27}$$

$$\begin{cases} x = \cos(\omega_R T_s) \\ y = \sin(\omega_R T_s). \end{cases} \tag{28}$$

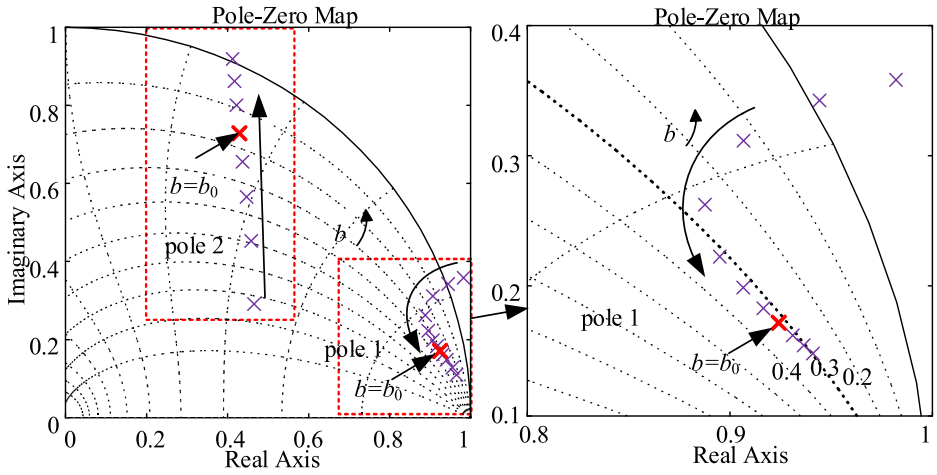


Fig. 11. Pole map of the closed-loop system varying with $b$ when $k_{\mathrm{p}} = 1$.

Setting the imaginary part of $T_{\mathrm{o}}(z)$ to be zero yields

$$AD - BC = 0. \tag{29}$$

Substituting (27)–(29) yields

$$(2x+1)(x-a)(1+\beta^2-2\beta x) = b(x-1)(1+\beta). \tag{30}$$

Substitute (29) to (26) and (26) can be simplified as

$$T_{\mathrm{o}}(e^{j\omega_R T_s}) \approx \frac{k_p(1-a)D}{B}. \tag{31}$$

Combining (27), (30), and (31) yields

$$T_{\mathrm{o}}(e^{j\omega_R T_s}) \approx \frac{k_p(1-a)(1+\beta)}{2(2x-\beta)(x-a)}. \tag{32}$$

$k_{\mathrm{pmax}}$ can be derived as

$$k_{p\max} = \frac{2(2x-\beta)(a-x)}{(1-a)(1+\beta)} \left(\frac{\beta}{2} < x < a\right). \tag{33}$$

As can be seen from (33), when $x = (2a+\beta)/4$, the upper limit $k_{\mathrm{pmax}}$ of $k_{\mathrm{p}}$ is maximized. Substituting $x = (2a+\beta)/4$ to (30) yields

$$b_0 = \frac{(2a+\beta+2)(2a-\beta)(2-2a\beta+\beta^2)}{4(4-2a-\beta)(1+\beta)} \tag{34}$$

$$k_{\mathrm{pmax}} = \frac{(2a-\beta)^2}{4(1-a)(1+\beta)}. \tag{35}$$

To illustrate that $b_0$ satisfies $0 < b_0 < b_{\max} = (2a-\beta)/(2-\beta)$, the curves of $b_0$ and $b_{\max}$ at different resonant frequencies are plotted in Fig. 9. Hence, the upper limit of $k_{\mathrm{p}}$ is maximized as $k_{\mathrm{pmax}}$, with $b$ setting to $b_0$, which means the closed-loop system is stable at the same time.

Fig. 10 shows the bode diagram of $T_{\mathrm{oz}}(z)$ with different $b$ at $k_{\mathrm{p}} = 1$. It can be observed in Fig. 10 that the amplitude margin of the system increases at first with the increasing of $b$, reaching the maximum at $b = b_0$, and then decreases. In other words, in the case of the same amplitude margin, the regions of $k_{\mathrm{p}}$ are the biggest at $b = b_0$, meaning that the dynamic performance of the system is best. Fig. 11 shows the pole map of the closed-loop system with different $b$ at $k_{\mathrm{p}} = 1$. There are two poles in the closed-loop system, among which pole 1 is introduced by the *CL* filter and pole 2 is introduced by the CVF loop. When damping coefficient $b$ is small, pole 1 is outside of the unit circle and the system is unstable, meaning that the active damping method cannot efficiently damp the resonance. With the increasing of $b$, pole 1 gradually moves into the unit circle, meaning that the *CL* filter resonance is well damped, while pole 2 gradually shifts from the inside of the unit circle to the outside of the unit circle at the same time. Hence, an excessive damping coefficient will make the system enter another unstable state. When $b = b_0$, pole 1 is located near the maximal damping line, and pole 2 keeps a sufficient distance from the boundary of the unit circle. Therefore, $b_0$ can be regarded as the optimal damping coefficient of the system.

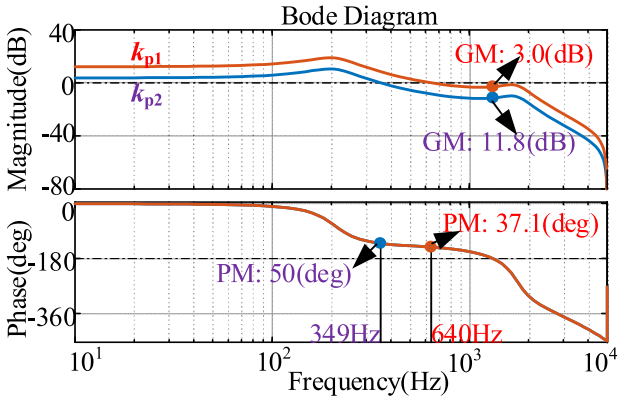


Fig. 12. Bode diagram of $T_{\mathrm{oz}}(z)$ with $k_{\mathrm{p1}}$ and $k_{\mathrm{p2}}$ at $b = b_0$.

As for the design of $k_{\mathrm{p}}$, the amplitude margin and the phase margin of the control system need to be considered comprehensively. In general, the amplitude margin of the control system is required to be greater than 3 dB and the phase margin is required to be located between 40° and 60°. In this article, the phase margin is adopted as 50°. To satisfy the requirement of the amplitude margin, $k_{\mathrm{p}}$ should satisfy

$$k_p \le k_{p1} = \frac{(2a-\beta)^2}{4\sqrt{2}(1-a)(1+\beta)}. \tag{36}$$

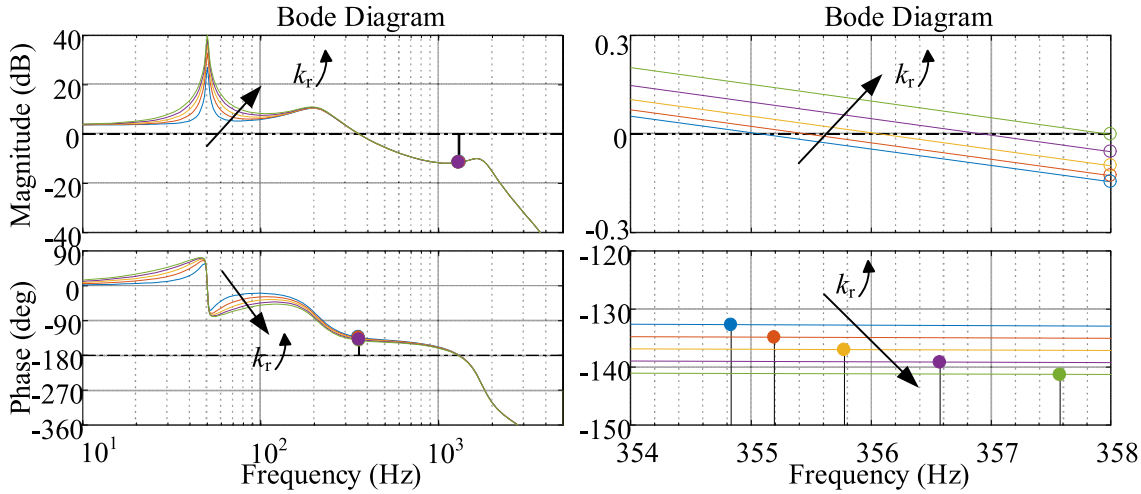


Fig. 13. Bode diagram of $T_{oz}(z)$ with different $k_r$.

As for the phase margin, it is required to utilize a bode diagram for analysis since there is no concise formula to express it. Assuming that the control system has a phase margin equal to or bigger than 50° at $k_p = k_{p2}$, the value of the $k_p$ is equal to min $\{k_{p1}, k_{p2}\}$.

Fig. 12 shows the bode diagram of $T_{oz}(z)$ with $k_{p1}$ and $k_{p2}$ at $b = b_0$. It can be observed in Fig. 12 that when $k_p = k_{p1}$, the amplitude margin is 3 dB and the phase margin is 37.1° with the system being stable; when $k_p = k_{p2}$, the amplitude margin is 11.8 dB and the phase margin is 50° with the system also being stable. For $k_{p2} < k_{p1}$, $k_{p2}$ should be chosen as the proportional coefficient of the PR controller.

Then, the design of the resonance coefficient $k_r$ of the PR controller is studied. Fig. 13 shows the bode diagram of $T_{oz}(z)$ with different $k_r$. As can be seen in Fig. 13, with the increasing of $k_r$, the steady-state gain of and the phase lag of the control system increases at the same time. The steady-state error will be smaller and the tracking accuracy will be higher with the increase in the steady-state gain. At the same time, the phase margin will be smaller and the robustness of the system will be worse with the increase in the phase lag. Hence, it is required to compromise the impacts of them when designing $k_r$. It can be observed in Fig. 13, when $k_r = 60$, the steady-state gain is 36.3 dB, the tracking error is 1.51%, the phase margin is 43.1°, and the bandwidth frequency is 721 Hz, which totally meet the requirements.

In a practical grid-connected CSI system, the actual resonant frequency of the *CL* filter may vary from the designed resonant frequency. Fig. 14 shows the impact of the resonant frequency $f_r$ on the poles position of the closed-loop system, when the cutoff frequency is equal to the designed the resonant frequency. It can be observed in Fig. 14 that the poles of the closed-loop system are still located in the unit circle with the change of $f_r$ from $0.5f_r$ to $1.5f_r$, which indicates that the system based on the proposed method has good robustness.

The procedure of the proposed parameter design method a grid-connect CSI system with proportional CVF-based active damping method can be summarized as follows.

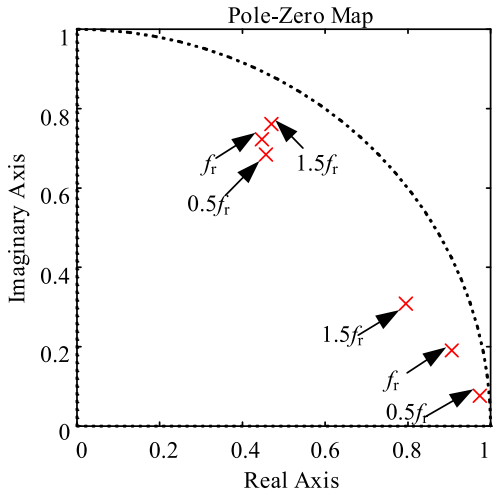


Fig. 14. Impact of $f_r$ on poles position of closed-loop system.

1) Calculate the resonant frequency $f_r$ of the target system and set the cutoff frequency of the high-pass filter utilized in the active damping loop to $f_r$.
2) Calculate the optimal damping coefficient $b$ according to (34), and derive the proportional CVF coefficient $H_s$ according to (18).
3) Calculate the proportional gain $k_{p1}$ with the amplitude margin being $-3$ dB, and derive $k_{p2}$ with the phase margin being 50° by the bode diagram. Then, $k_p$ is obtained as the smaller one of $k_{p1}$ and $k_{p2}$.
4) Derive the resonance gain $k_r$ by the bode diagram considering both the steady-state error and the stability margin.

Fig. 15 depicts the control strategy of the grid-connected CSI system with a proportional CVF-based active damping method. Firstly, the $d$-axis reference $i_d{}^*$ of the grid-connected current is derived by the difference between dc-side current and its reference calculated by the PI controller. The $q$-axis reference $i_q{}^*$ of the grid-connected current is equal to 0. Then the current reference $i_{dq}{}^*$ is transformed by Park's transformation to the

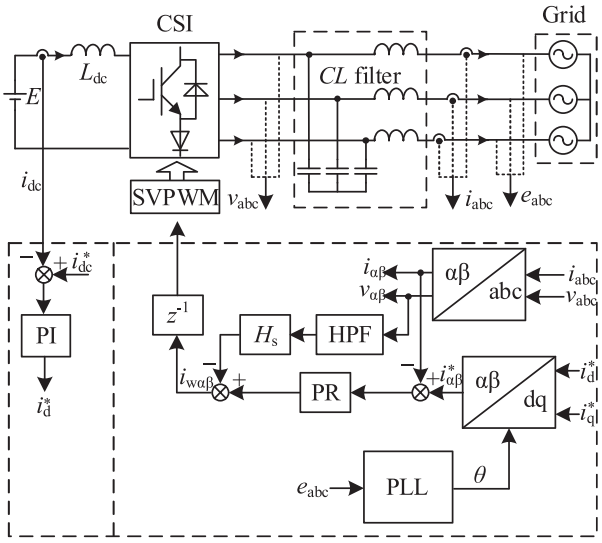


Fig. 15. Control strategy of the grid-connected CSI system with proportional CVF-based active damping method.

TABLE II
PARAMETERS OF THE GRID-CONNECTED CSI SYSTEM

| Symbol | Description | Value |
|---|---|---|
| $E_{dc}$ | Inverter dc voltage | 140V |
| $e_g$ | Grid phase-phase voltage | 110V(RMS) |
| $f_B$ | Grid voltage frequency | 50Hz |
| $L_{dc}$ | DC inductance | 12mH |
| $C$ | Filter capacitance | 50$\mu$F |
| $L$ | Filter inductance | 3mH |
| $f_s$ | Sampling frequency | 10kHz |
| $H_s$ | Optimal proportional feedback coefficient | 0.332 |
| $k_p$ | Proportional gain of PR controller | 1.48 |
| $k_r$ | Resonant gain of PR controller | 60 |

current reference $i_{\alpha\beta}{}^*$ in the stationary system. The difference between the reference and the sampling of grid-connected current in the stationary system calculated by the PR controller pluses the proportional CVF term and the reference $i_{w\alpha\beta}$ of the inverter-side is obtained. Finally, the reference $i_{w\alpha\beta}$ is utilized by SVPWM to derive IGBT driving signals.

## V. SIMULATION RESULT

In order to verify the effectiveness of the proposed method in this article, a detailed model of the three-phase grid-connected CSI system is established in MATLAB/Simulink. The parameters of the target system are shown in Table II.

Fig. 16 compares the start-up response of the system for cases with a different cutoff frequency of the high-pass filter in CVF loop, when RMS of phase voltage is equal to 110 V.

It can be observed in Fig. 16(a) that the waveform of the dc-side current is overshot when the system starts up and takes a long time to enter the steady state, for the proportional CVF coefficient is larger than the output of the PR controller when high-pass filter is not utilized in CVF loop. In the case that the high-pass filter is utilized in the CVF loop, as shown in Fig. 16(b) and (c), the overshot of the dc-side current is limited. However, it takes a longer time to enter a steady state when

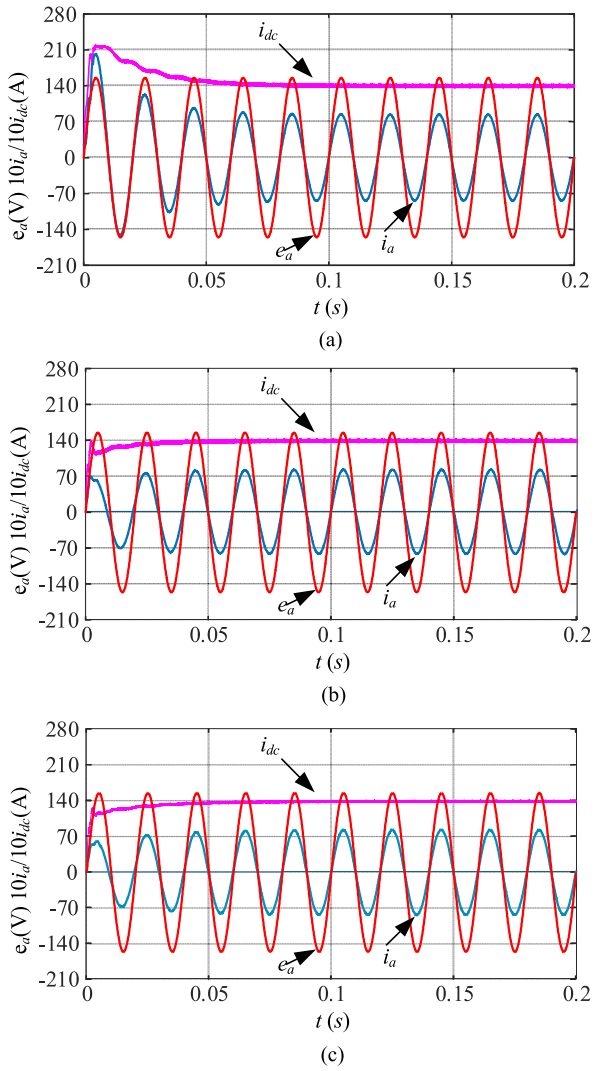


Fig. 16. Simulation results of start-up response when RMS of grid voltage is equal to 110 V. (a) $\omega_c = 0$. (b) $\omega_c = \omega_r$. (c) $\omega_c = 2\omega_r$.

the cutoff frequency of the high-pass filter $\omega_c$ takes a lager value, comparing Fig. 16(b) and (c). The impact shown above is more serious when the grid voltage is larger, which means that the fundamental component of the capacitance voltage and the feedback of the capacitor voltage is larger. Fig. 17 shows the start-up response of the system when the RMS of phase voltage is equal to 150 V compared to Fig. 16. It can be observed that with the larger grid phase voltage, the starting-up over-shoot of dc-side current becomes larger and the dynamics of the system become worse comparing Figs. 16(a) and 17(a). Meanwhile, the results of Figs. 16(b) and 17(b) illustrate that with a high-pass filter utilized in the CVF loop, the grid phase voltage has hardly an impact on the start-up performance of the system. In such a case, the overshoot of the dc-side current is small. The overshoot can be better limited when $\omega_c = 2\omega_r$, but the dynamics may be worse at the same time, as can be seen from Fig. 17. Hence, $\omega_c = \omega_r$ is adopted in this article.

The results of Figs. 18 and 19 illustrate that the damping coefficient must be selected properly to mitigate the *CL* resonance

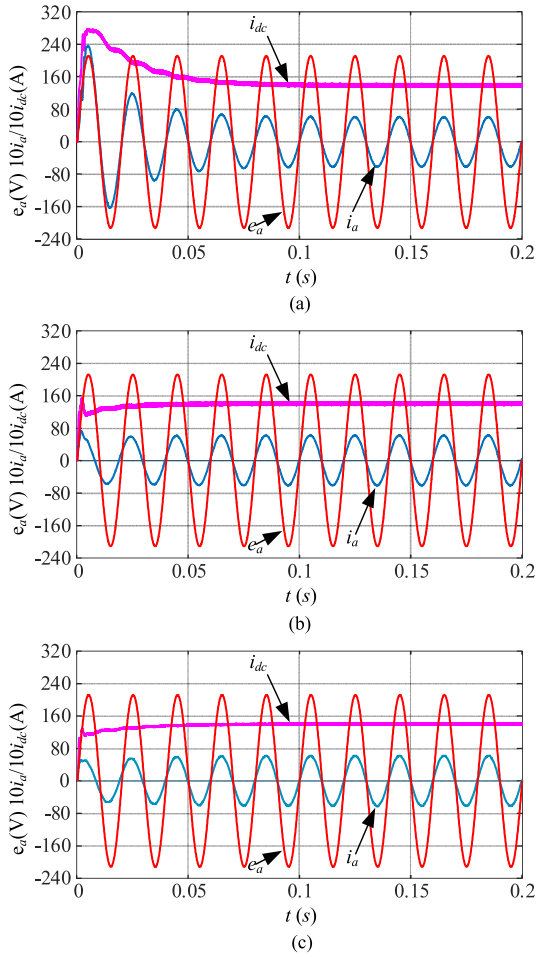


Fig. 17. Simulation results of start-up response when RMS of grid voltage is equal to 150 V. (a) $\omega_c = 0$. (b) $\omega_c = \omega_r$. (c) $\omega_c = 2\omega_r$.

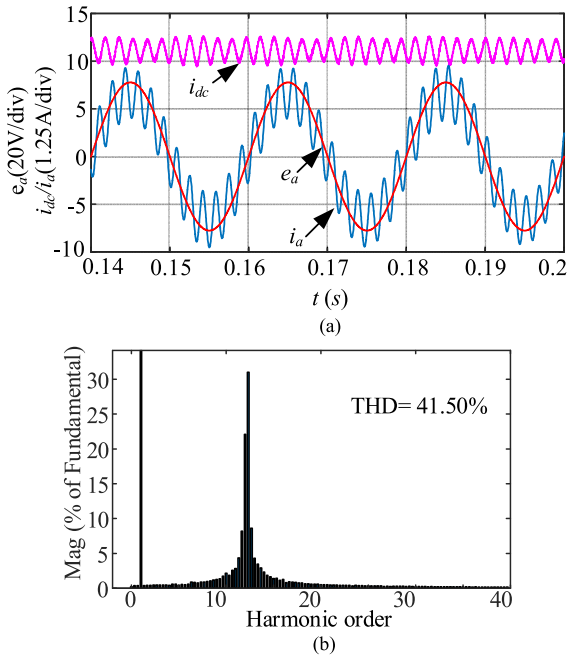


Fig. 18. Simulation results with a small damping coefficient $H_s = 0.067$. (a) Waveforms. (b) FFT analysis of grid-connected current.

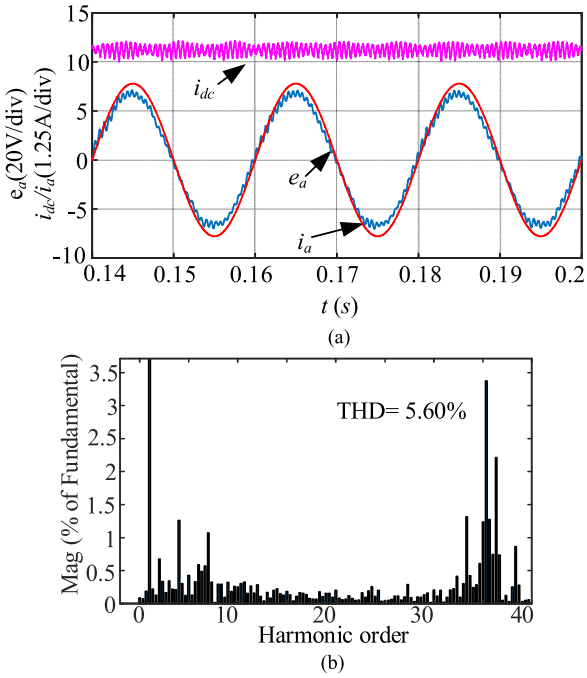


Fig. 19. Simulation results with a big damping coefficient $H_s = 0.421$. (a) Waveforms. (b) FFT analysis of grid-connected current.

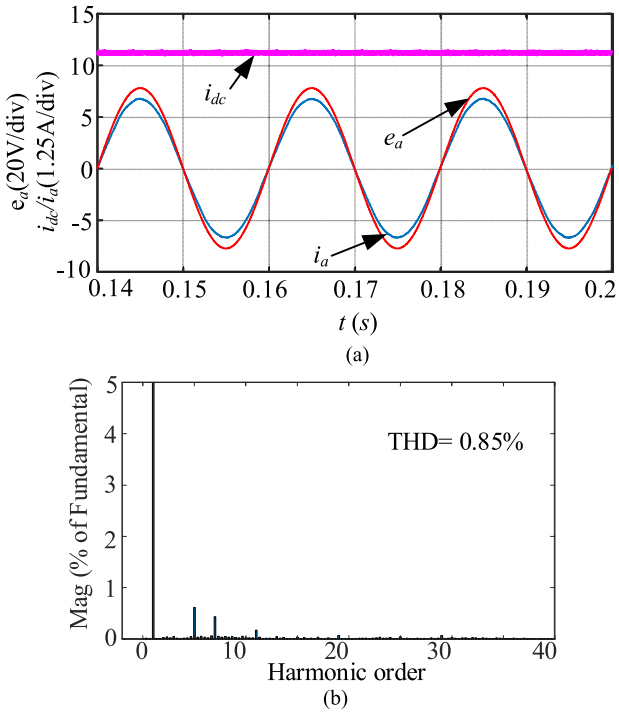


Fig. 20. Simulation results with optimal damping coefficient $H_s = 0.332$. (a) Waveforms. (b) FFT analysis of grid-connected current.

effectively. Fig. 20 shows the simulation results when $H_s = 0.332$, which is derived from the optimal damping coefficient obtained by the proposed method in this article. The results show that the *CL* resonance is effectively mitigated and the THD of grid-connected current is 0.85% with the good steady-state

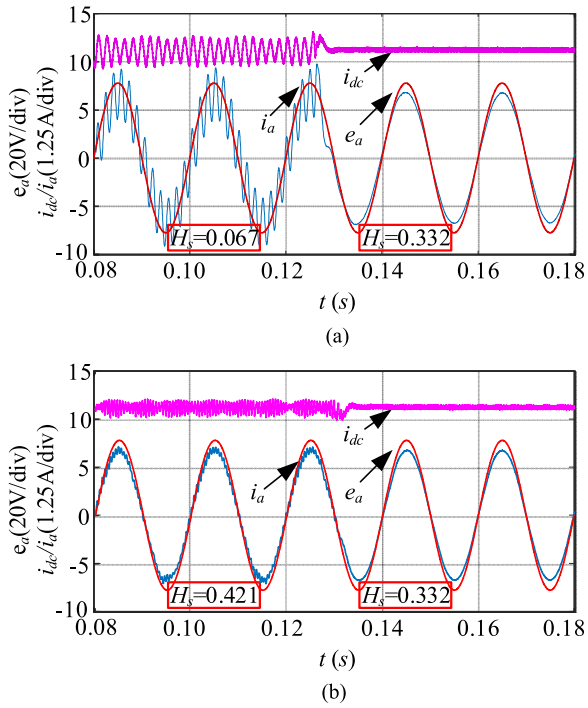


Fig. 21. Simulation results with the damping coefficient changing. (a) From a small one to the optimal. (b) From a large one to the optimal.

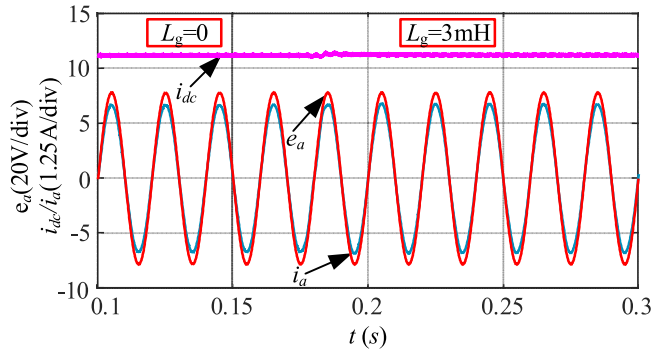


Fig. 22. Simulation results with $L$g changing.

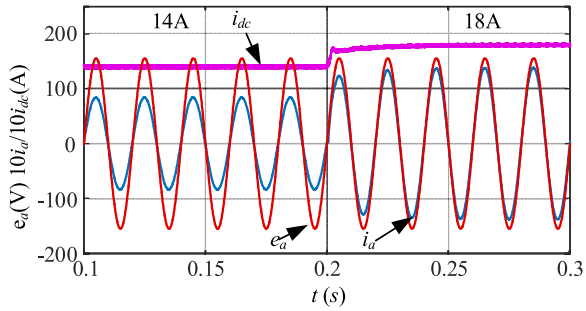


Fig. 23. Simulation results of transient response of the system.

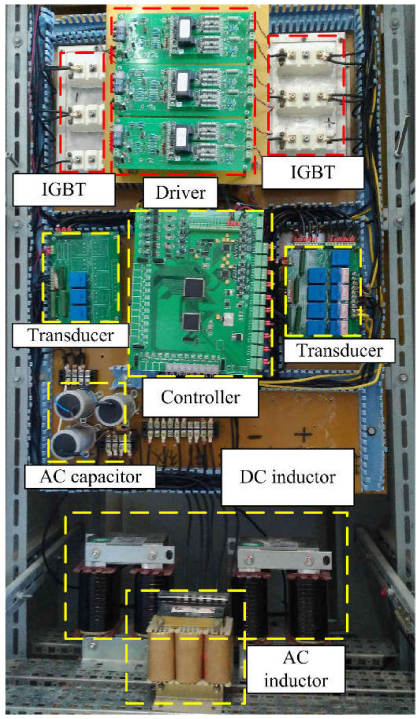


Fig. 24. Three-phase CL-filtered grid-connected CSI system used in the experiment.

waveform quality, which verifies the effectiveness of the theoretical analysis and the parameters design method in this article. The simulation results of the target system with the damping coefficient changing are shown in Fig. 21. It can be observed from Fig. 21 that, with the damping coefficient changing from the nonoptimal to the optimal, the *CL* resonance is mitigated immediately.

In a practical grid-connected CSI system, grid impedance may exist between the terminal of CSI and the ideal grid and the value of the resonant frequency may vary from the designed value because of the existence of grid impedance. Grid impedance is usually inductive and we use $L_g$ to represent it. Fig. 22 shows the simulation results when $L_g$ varies from 0 to 3 mH. It can be observed that the system can remain stable with the variation of $L_g$, which means that the system is robust under the designed parameters.

Fig. 23 shows the transient response of the system, in case that reference of dc-side current shifts from 14 to 18 A at 0.2 s, which show that the system can track the current reference without error after two or three fundamental frequency periods with small overshoot.

According to the simulation results, a high-pass filter in the damping loop can mitigate the start-up overshoot of dc-side current and improve the dynamics in the grid-connected CSI system with proportional CVF active damping. However, the value of the cutoff frequency of high-pass filter should not be too large to affect the dynamics and damping performance.

## VI. Experimental Results

To further verify the effectiveness of the proposed method, a three-phase grid-connected CSI system is constructed as shown in Fig. 24. The parameters of the system are the same as those listed in Table II. The CSI is controlled by

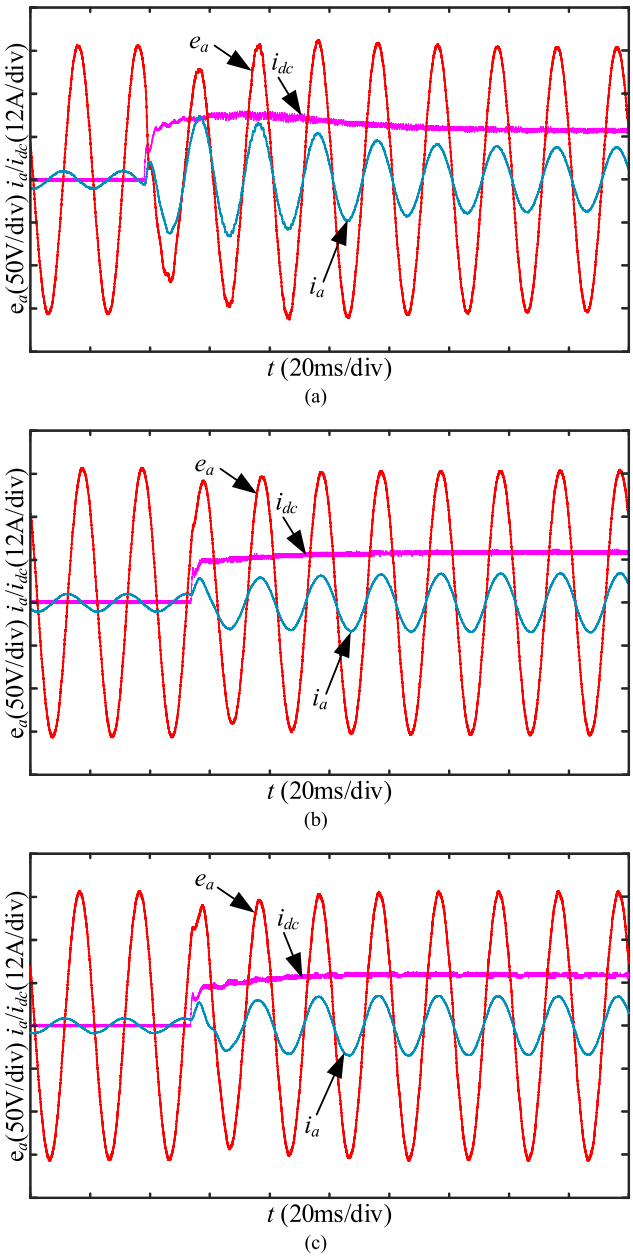


Fig. 25. Experiment of start-up response when rms of grid voltage is equal to 110 V. (a) $\omega_c = 0$. (b) $\omega_c = \omega_r$. (c) $\omega_c = 2\omega_r$.

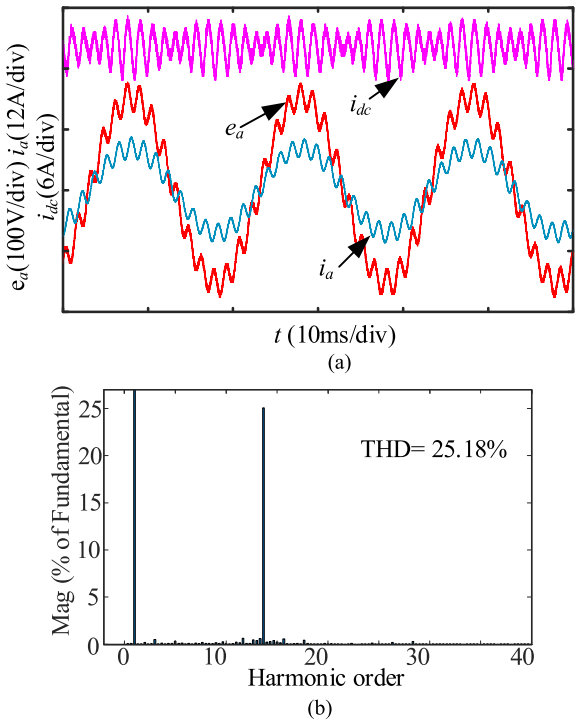


Fig. 26. Experimental results with a small damping coefficient $H_s = 0.067$. (a) Waveforms. (b) FFT analysis of the grid-connected current.

DSP (TMS320F28335) along with field programmable gate array (XC3S400). The IGBT power modules utilized the BSM50GB120DLC made by Infineon. In order to make the IGBT modules have reverse voltage withstand capability, a freewheeling diode of the same type of IGBT module is utilized in series with each IGBT module. The drive module is the IGBT drive module CONCEPT SCALE DRIVER 2SD315AN.

Fig. 25 shows the experimental results of the start-up response of the target system when the rms of grid voltage is equal to 110 V. It can be observed in Fig. 25(a) that the waveform of the dc-side current is overshot when the system starts up and takes a long time to enter the steady state. When utilizing the high-pass filter in the CVF loop, the overshoot of dc-current is limited and the system enters the steady-state quickly, as shown in Fig. 25(b) and (c). However, it will take the control system more time to enter a steady state when the value of the cutoff frequency of the high-pass filter is large. The results of Fig. 25 illustrate that utilizing a high-pass filter in the damping loop is necessary for a grid-connected CSI system with a proportional CVF-based active damping method, which is consistent with the simulation results.

Figs. 26–28 show the experimental results of the waveforms of the system with three different damping coefficients. It can be observed in Fig. 26 that the system oscillates at a low frequency near the 12th-order fundamental frequency when $H_s = 0.067$, which indicates that the *CL* resonance is not sufficiently mitigated when the damping coefficient is small.

The results in Fig. 27 show that the system oscillates at a high frequency near the 33th-order fundamental frequency when $H_s = 0.421$, which indicates the target system remains unstable. The experimental results shown in Figs. 26 and 27 are in accordance with the theoretical analysis in Section IV, i.e., the increase in the damping coefficient converts the poles of the closed-loop system from a critical stable point of the low oscillation frequency to another critical stable point of the high oscillation frequency. Fig. 28 shows the experimental results with the optimal damping coefficient, when $H_s = 0.332$. In such a case, the *CL* resonance is effectively mitigated with the THD of the grid-connected current equal to 2.30%, which satisfies the requirements of grid-connected current.

Fig. 29 shows the experimental results of the target system with the damping coefficient changing. It can be observed in Fig. 29 that the *CL* resonance can be mitigated immediately

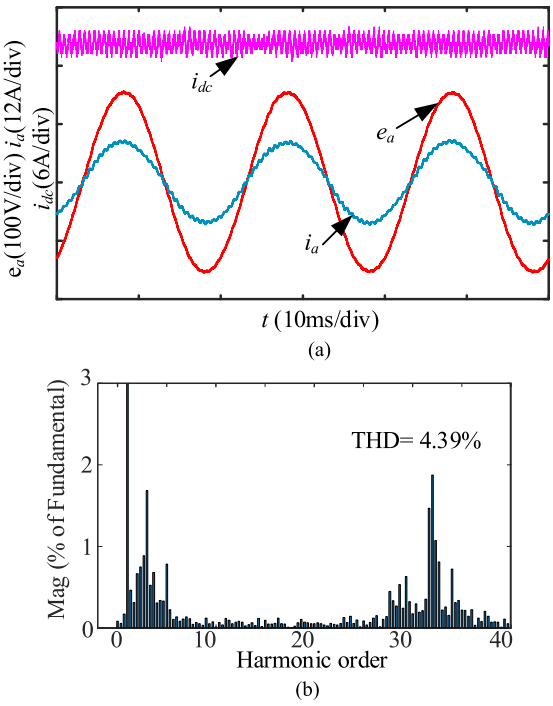


Fig. 27. Experimental results with a big damping coefficient $H_s = 0.421$. (a) Waveforms. (b) FFT analysis of the grid-connected current.

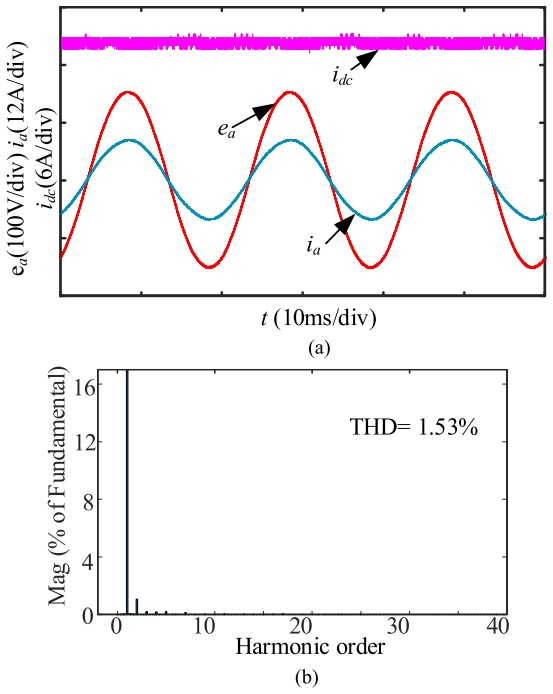


Fig. 28. Experimental results with optimal damping coefficient $H_s = 0.332$. (a) Waveforms. (b) FFT analysis of the grid-connected current.

when the damping coefficient changes from a nonoptimal one to the optimal, which is the same as the simulation analysis. Fig. 30 shows the experimental results when the grid impedance $L_g$ is equal to 3 mH, which may exist between the terminal of CSI and ideal grid and change the resonant frequency of the

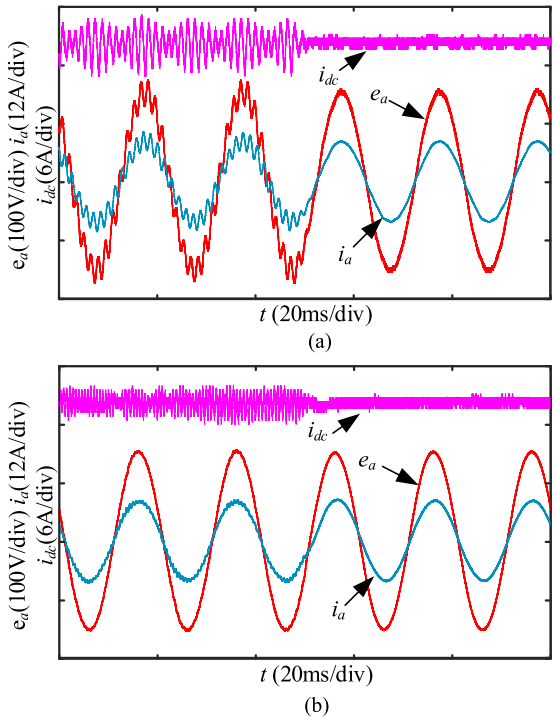


Fig. 29. Experimental results with the damping coefficient changing. (a) From a small one to the optimal. (b) From a large one to the optimal.

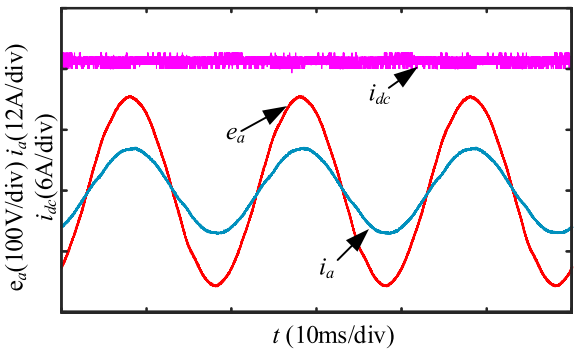


Fig. 30. Experimental results when $Lg = 3$ mH.

system. It can be observed in Fig. 30 that the system can remain stable under designed parameters.

Fig. 31 shows the experimental results of the transient response of the system, in the case that reference of dc-side current shifts from 14 to 18 A at 0.2 s. It can be seen in Fig. 31 that the system can track the current reference without error after 2 or 3 fundamental frequency periods with small overshoot.

The experimental results of the grid-connect CSI system provided a further verification of the analysis in this article.

1) A high-pass filter utilized in the damping loop a grid-connected CSI system with a proportional CVF-based active damping method can mitigate the overshoot of start-up current and improve start-up dynamics of the system.
2) A small or a big damping coefficient cannot mitigate the CL resonance of the system. The optimal damping

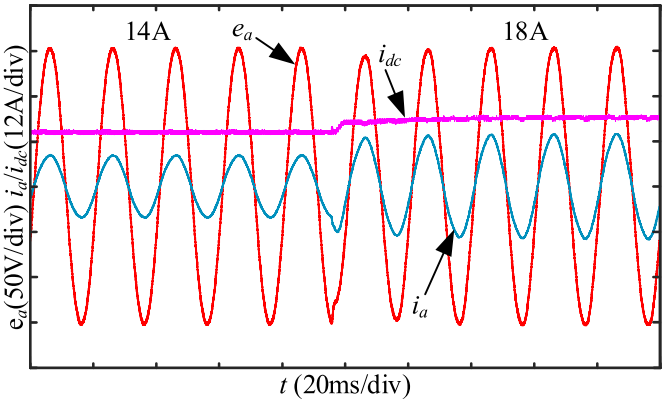


Fig. 31. Experimental results of transient response of the system.

coefficient based on the proposed method can damp the resonance sufficiently.

3) With the proposed parameters design method, in this article, the system has good steady-state performance and dynamics.

## VII. Conclusion

In a grid-connected CSI system with a proportional CVF active damping method, a high-pass filter was usually utilized in the damping loop to mitigate the impacts of the damping loop on the dynamics of the system. In such a case, the following work was accomplished in this article.

1) Considering the impacts of high-pass filter and control delay, the detailed impacts of the cutoff frequency of the high-pass filter and damping coefficient on the system stability was analyzed in the discrete domain, and the effective regions of damping coefficient were obtained.
2) The relationship between damping coefficient, controller, and system stability was studied and a key parameter design method of the control system was proposed. First, derive the optimal damping coefficient based on the principle of maximizing regions of the proportionality of the PR controller. Then, design the parameters of the PR controller considering the amplitude margin and the phase margin of the system. The proposed method simplified the procedure of designing the key parameters of the control, which can effectively mitigate the *CL* resonance with good robust performance, steady-state performance, and dynamics.
3) Simulation and experimental results verified the effectiveness of the analysis and parameter design of the control system in this article.

## References

[1] E. Lorenzani, F. Immovilli, G. Migliazza, M. Frigieri, C. Bianchini, and M. Davoli, "CSI7: A modified three-phase current-source inverter for modular photovoltaic applications," *IEEE Trans. Ind. Electron.*, vol. 64, no7, pp. 5449–5459, Jul. 2017.

[2] H. Wu, Y. Liu, and Z. Wang, "Implementation of a new high-power current-source single-stage PV grid-connected system with reactive power compensation," *IET Renewable Power Gener.*, vol. 13, no. 11, pp. 1873–1881, Aug. 2019.

[3] Q. Wei, B. Wu, D. Xu, and N. R. Zargari, "Natural sampling SVM-based common-mode voltage reduction in medium-voltage current source rectifier," *IEEE Trans. Power Electron.*, vol. 32, no. 10, pp. 7553–7560, Oct. 2017.

[4] Y. W. Li, M. Pande, N. R. Zargari, and B. Wu, "DC-link current minimization for high-power current-source motor drives," *IEEE Trans. Power Electron.*, vol. 24, no. 1, pp. 232–240, Jan. 2009.

[5] A. Terciyanli, M. Ermis, and I. Cadirci, "A selective harmonic Amplification method for reduction of kVA rating of current source converters in shunt active power filters," *IEEE Trans. on Power Del.*, vol. 26, no.1, pp. 65–78, Jan. 2011.

[6] M. Salo and H. Tuusa, "A vector controlled current-source PWM rectifier with a novel current damping method," *IEEE Trans. Power Electron.*, vol. 15, no. 3, pp. 464–470, May 2000.

[7] Y. W. Li, B. Wu, N. Zargari, J. Wiseman, and D. Xu, "An effective method to suppress resonance in input LC filter of a PWM current-source rectifier," in *Proc. CES/IEEE 5th Int. Power Electron. Motion Control Conf.*, 2006, pp. 1–6.

[8] M. Mao, S. Weng, F. Liu, L. Chang, M. Ding, and H. Wu, "A novel PRD control method damping resonance in grid-connected three-phase SVPWM current source inverter," in *Proc. 3rd IEEE Int. Symp. Power Electron. Distrib. Gener. Syst.*, 2012, pp. 487–491.

[9] Y. Neba, "A simple method for suppression of resonance oscillation in PWM current source converter," *IEEE Trans. Power Electron.*, vol. 20, no. 1, pp. 132–139, Jan. 2005.

[10] X. Wang, Y. W. Li, F. Blaabjerg, and P. C. Loh, "Virtual-impedance-based control for voltage-source and current-source converters," *IEEE Trans. Power Electron.*, vol. 30, no. 12, pp. 7019–7037, Dec. 2015.

[11] M. H. Bierhoff and F. W. Fuchs, "Active damping for three-phase PWM rectifiers with high-order line-side filters," *IEEE Trans. Ind. Electron.*, vol. 56, no. 2, pp. 371–379, Feb. 2009.

[12] Z. Bai, H. Ma, D. Xu, B. Wu, Y. Fang, and Y. Yao, "Resonance damping and harmonic suppression for grid-connected current-source converter," *IEEE Trans. Ind. Electron.*, vol. 61, no. 7, pp. 3146–3154, Jul. 2014.

[13] H. Gao, B. Wu, D. Xu, and N. R. Zargari, "A model predictive power factor control scheme with active damping function for current source rectifiers," *IEEE Trans. Power Electron.*, vol. 33, no. 3, pp. 2655–2667, Mar. 2018.

[14] F. Liu, B. Wu, N. R. Zargari, and M. Pande, "An active damping method using inductor-current feedback control for high-power PWM current-source rectifier," *IEEE Trans. Power Electron.*, vol. 26, no. 9, pp. 2580–2587, Sep. 2011.

[15] X. Zhang, J. W. Spencer, and J. M. Guerrero, "Small-signal modeling of digitally controlled grid-connected inverters with LCL filters," *IEEE Trans. Ind. Electron.*, vol. 60, no. 9, pp. 3752–3765, Sep. 2013.

[16] D. G. Holmes, T. A. Lipo, B. P. McGrath, and W. Y. Kong, "Optimized design of stationary frame three phase AC current regulators," *IEEE Trans. Power Electron.*, vol. 24, no. 11, pp. 2417–2426, Nov. 2009.

[17] Y. Geng, Y. Yun, R. Chen, K. Wang, H. Bai and X. Wu, "Parameters design and optimization for LC-type off-grid inverters with inductor-current feedback active damping," *IEEE Trans. Power Electron.*, vol. 33, no. 1, pp. 703–715, Jan. 2018.

[18] Y. Li, L. Ding, and Y. W. Li, "Isomorphic relationships between voltage-source and current-source converters," *IEEE Power Electron. Lett.*, vol. 34, no. 8, pp. 7131–7135, Aug. 2019.

[19] Y. W. Li, "Control and resonance damping of voltage-source and current-source converters with LC filters," *IEEE Trans. Ind. Electron.*, vol. 56, no. 5, pp. 1511–1521, May 2009.

[20] Y. Zhang, Y. Yi, P. Dong, F. Liu, and Y. Kang, "Simplified model and control strategy of three-phase PWM current source rectifiers for DC voltage power supply applications," *IEEE J. Emerg. Sel. Topics Power Electron.*, vol. 3, no. 4, pp. 1090–1099, Dec. 2015.

[21] Q. Guo, H. Liu, and Y. Zhang, "A new control strategy for a three-phase PWM current-source rectifier in the stationary frame," *J. Power Electron.*, vol. 15, no. 4, pp. 994–1005, Jul. 2015.

[22] Q. Guo, H. Liu, P. Dong, P. Liu and Y. Zhang, "A novel control strategy and its parameter design of the current-loop in a stationary frame for current-source PWM rectifiers," *Chin. Soc. Elect. Eng.*, vol. 34, no. 15, pp. 2353–2361, May 2014.

[23] C. Bao, X. Ruan, X. Wang, W. Li, D. Pan, and K. Weng, "Step-by-step controller design for LCL-type grid-connected inverter with capacitor current-feedback active-damping," *IEEE Trans. Power Electron.*, vol. 29, no. 3, pp. 1239–1253, Mar. 2014.

**Yiwen Geng** was born in Jiangsu Province, China, in 1977. He received the B.S., M.S., and Ph.D. degrees from the School of Electrical and Power Engineering, China University of Mining and Technology, Xuzhou, China, in 2000, 2004, and 2014 respectively.

From 2006 to 2016, he was a Lecturer with the School of Electrical and Power Engineering, China University of Mining and Technology. Since 2016, he has been with the Department of School of Electrical and Power Engineering, China University of Mining and Technology, where he is currently an Associate Professor. His current research interests include power electronic stability and electric vehicle drive control.

**Xuanfeng Song** was born in Guangxi, China, in 1995. He received the B.S. degree in material science and engineering from Southeast University, Nanjing, China, in 2017. He is currently working toward the M.S. degree with the School of Electrical and Power Engineering, China University of Mining and Technology, Xuzhou, China.

His research interests include distributed generation system stability analysis and control.

**Ke Yang** was born in Jiangsu Province, China, in 1995. He received the B.S. degree in building electrical and intelligent from the Yang Zhou University, Yangzhou, China, in 2017. He is currently working toward the M.S. degree in electrical engineering at the School of Electrical and Power Engineering, China University of Mining and Technology, Xuzhou, China.

His current research interests include the control of current-source converters and its topology.

**Xu Zhang** was born in Shandong Province, China, in 1996. He received the B.S. degree in electrical engineering and automation, in 2018, from the China University of Mining and Technology, Xuzhou, China, where he is currently working toward the M.S. degree in electrical engineering with the School of Electrical and Power Engineering.

His current research interests include the control of current-source converters and its topology.

**Haiwei Liu** was born in Jiangsu Province, China, in 1994. He received the B.S. degree in electrical engineering, in 2016, from the China University of Mining and Technology, Xuzhou, China, where he is currently working toward the M.S. degree in electrical engineering with the School of Electrical and Power Engineering.

His current research interests include the control strategy and topology of current-source converters.